Disruption of Ordered Membrane Domains as a Mechanism Underlying Neuropathic Pain

Lucas J. Handlin[1], Natalie L. Macchi[1], Nicolas Dumaire[2,3], Lyuba Salih[2,3], Kyle S. McCommis[1], Aubin Moutal[2,3], and Gucan Dai[1,3,*]

Author Affiliations

[1]Edward A. Doisy Department of Biochemistry and Molecular Biology,
[2]Department of Pharmacology and Physiology,
[3]Institute for Translational Neuroscience,
Saint Louis University School of Medicine, 1100 South Grand Blvd., St. Louis, MO, USA 63104
*Correspondence: Gucan Dai (email: gucan.dai@health.slu.edu)

Abstract

Cell membranes consist of heterogeneous lipid domains that influence key cellular processes, including signal transduction, endocytosis, and electrical excitability. The goal of this study was to assess the size of cholesterol-enriched ordered membrane domains (OMD) in various cell types. Multiple cell types were tested using fluorescence lifetime imaging microscopy (FLIM) and Förster resonance energy transfer (FRET), whereby small nociceptor DRG neurons and cardiac pacemaker cells displayed the highest FRET intensities. This implies that electrically active cells tend to have large OMDs. Treatment of cells with the cholesterol-extracting reagent β-cyclodextrin (β-CD) led to a decrease in FRET, indicating a reduction in the OMD size, whereas detergents known to promote domain coalescence in artificial membranes increased OMD size. In an *in vitro* fatty liver model, palmitate supplementation increased FRET whereas oleate supplementation decreased FRET in isolated primary murine hepatocytes, highlighting the importance of unsaturated lipid tails in lipid domain organization. Disruption of OMD using β-CD potentiated action potential firing in nociceptor DRG neurons and decreased the free energy needed for opening native hyperpolarization-activated cyclic nucleotide-gated (HCN) channels. After disrupting the OMD, HCN channels exhibited an increased relative open probability at the resting membrane potential (RMP). A significant reduction in FRET was observed in both a chemotherapy-induced neuropathic pain model and a spared nerve injury model of neuropathic pain, consistent with disrupted or shrunken OMD in these models. Collectively, these findings show that disturbances in lipid domains may contribute to the progression of neuropathic pain, and they suggest new therapeutic strategies to achieve pain relief.

Introduction

Membrane lipids form distinct compartments known as lipid domains, which serve as specialized regions within cell membranes for localized cell signaling. Within these domains, a specific type called detergent-resistant lipid-ordered membrane domains (OMDs) has attracted significant attention (1-3). OMDs differ from other regions, such as the disordered membrane domains (DMDs), due to their unique composition enriched with cholesterols and sphingolipids. The OMDs possess an intriguing characteristic of varying in size, ranging from a few nanometers to hundreds of nanometers. This dynamic nature allows the lipid domains to undergo rapid changes, coalescing or splitting apart, in response to different physiological conditions. To unravel the function and structure of these lipid domains within cellular systems, techniques such as super-resolution microscopy, single-molecule fluorescence, and cryo-electron tomography have been used to visualize and characterize these structured domains (4-6). Nevertheless, many details about the structure, function, and significance of OMDs remain elusive.

The significance of lipid domains has been recognized in diverse biological processes. For instance, in Alzheimer's disease, the dysregulation of lipid domains has been implicated in the accumulation of amyloid-β plaques (7-9). In viral infections, these domains can serve as entry sites for the viruses into cells (10, 11). Inflammatory responses involve the reorganization of lipid domains, influencing cell signaling and immune responses. Moreover, emerging evidence suggests a link between lipid domains and chronic pain, particularly neuropathic pain that is often caused by nerve injuries (12, 13). In an animal model of chemotherapy-induced peripheral neuropathy and arthritis, targeting of lipid domains was effective to alleviate the pathological symptoms (14). However, the connection between OMDs and neuropathic pain remains understudied. Manipulating these domains may hold potential for developing targeted treatments for diseases related to lipid domain dysfunction, including neurodegenerative disorders, viral infections, inflammatory conditions, and neuropathic pain.

Pacemaker hyperpolarization-activated cyclic nucleotide-gated (HCN) channels play critical roles in several important physiological processes (15). These channels are involved in establishing the resting membrane potential (RMP) and regulating the frequency of action potentials, thereby contributing to the automaticity of excitable cells (15). Moreover, HCN channels are important for pain sensation, as evidenced by their involvement in repetitive firing of primary nociceptor neurons in the dorsal root ganglion (16-18). HCN2-channel current is responsible for eliciting repetitive firing in nociceptor neurons (19, 20). In support of this, knocking out the HCN2 gene reduces neuropathic pain

in animals (16, 21). Conversely, increased HCN channel activity correlates with spontaneous action potential firing and chronic pain, while pharmacological blockade of HCN channel activity decreases inflammatory and neuropathic pain (16, 18, 22). Moreover, the lipid domain-specific localization of HCN channels appears to significantly influence their function and thereby the neuronal and cardiac excitability (23-25). The function of cardiac HCN4 channels depends on compartmentalized cAMP signaling in lipid microdomains (26, 27). We showed that the voltage-sensing process of HCN channels, including the voltage-sensor movement, is directly regulated by OMDs (28). In addition, the voltage-sensing modules of HCN channels interact intimately with membrane lipids, including signaling phosphoinositides (29-32). In summary, these studies corroborate a significant connection between pain sensation and the regulation of pacemaker HCN channels by membrane lipids.

In this current study, we performed fluorescence lifetime imaging microscopy (FLIM) and Förster resonance energy transfer (FRET), which are well-suited for evaluating the nanometer sized OMDs in various cell types. Nociceptor DRG neurons exhibit larger OMDs than non-nociceptive DRG neurons. When the OMD is disrupted, the action potential firing of nociceptor DRG neurons becomes more frequent. In addition, we found that HCN2 channels, abundantly expressed in nociceptor DRG neurons, tend to localize within the OMD and are sensitive to the disruption of lipid domains. Furthermore, significant reductions in FLIM-FRET were observed in both a chemotherapy-induced neuropathic pain model and a nerve injury-induced model of neuropathic pain, suggesting diminished OMD sizes in these pain models. These findings strongly suggest that perturbations in lipid domains and a resulting increase in the HCN channel opening near the RMP contribute to the mechanisms underlying neuropathic pain.

Results

Imaging the OMDs of living cells using FLIM-FRET and cholera toxin subunit B

We employed cholera toxin subunit B (CTxB)-conjugated FRET donors and acceptors as probes to investigate lipid nanodomains. CTxB, derived from *Vibrio cholerae,* acts as a pentameric multivalent ligand with exceptionally high affinity (picomolar) for GM1 gangliosides (33, 34). These gangliosides, specifically GM1, are distinct sphingolipid molecules that are prominently present in OMDs. Conventional fluorescence microscopy encounters limitations due to the diffraction limit of light (250 nm), often making it impossible to visualize small-sized lipid domains. FRET-based fluorescence microscopy can overcome this limitation by acting as a spectroscopic distance ruler with nanometer

sensitivity. This sensitivity is ideal for detecting nanoscale lipid domains of the dimensions thought to be critical in biological membranes (35). We used Alexa Fluor 488 (AF-488) CTxB conjugates as FRET donors with Alexa Fluor 647 (AF-647) CTxB conjugates serving as FRET acceptors (Fig. 1A). This specific FRET pair was previously established, with an Förster critical distance (R_0) value of approximately 52 Å (36). As the size of lipid domains exceeds a radius of approximately 15 nm, the likelihood of accommodating two CTxB pentamers within the same lipid domain becomes significantly higher (34). In contrast, when the lipid domain has a radius of less than 10 nm, it can accommodate only one CTxB pentamer (34), resulting in minimal FRET between AF-488 and AF-647. Accordingly, this approach can effectively quantify the relative size of lipid domains.

Figure 1

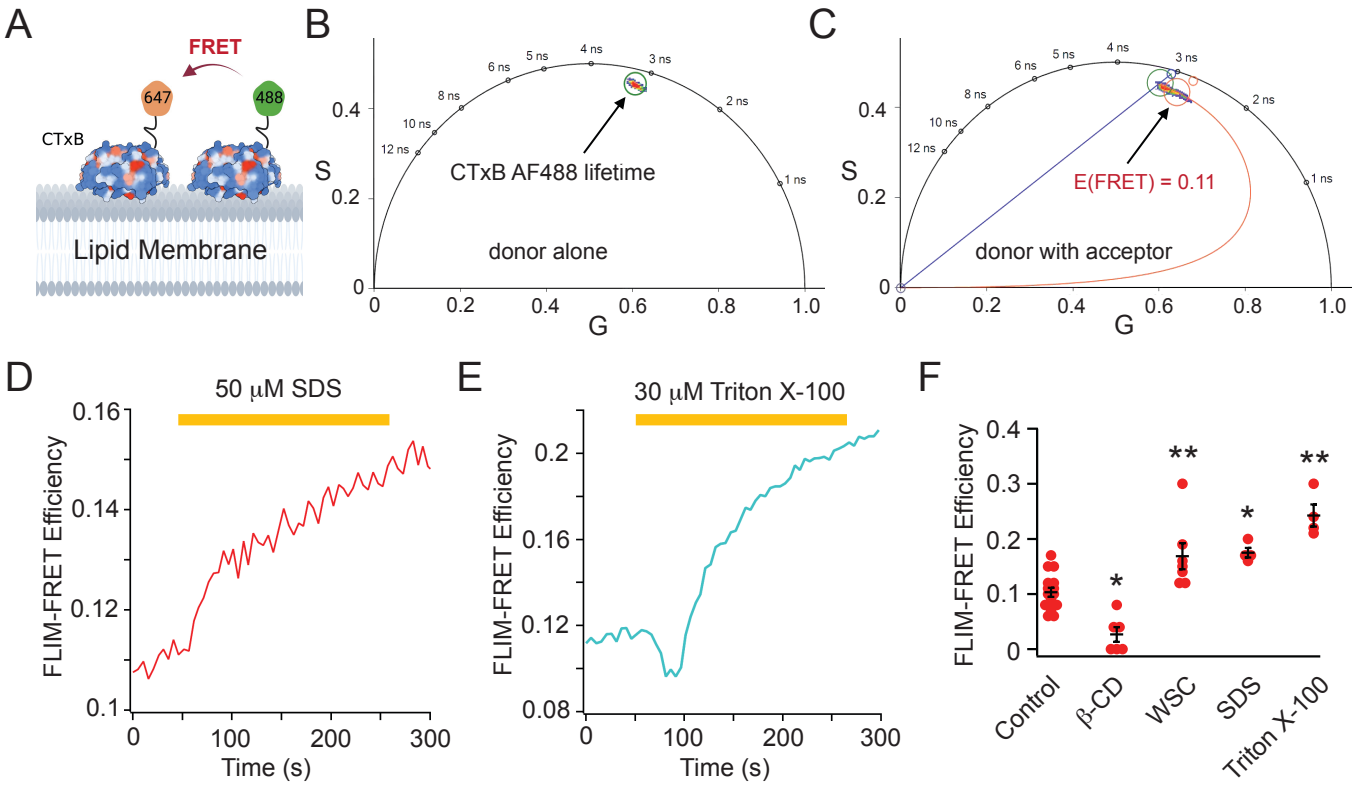

Figure 1. Assessing the OMD size using FLIM-FRET and cholera toxin conjugated FRET pairs. (**A**) Experimental design using the FRET donor CTxB-AF 488 together with the FRET acceptor CTxB-AF 647. (**B-C**) Representative phasor plots of tsA201 cells labeled by donor alone (CTxB-AF 488) or together with the FRET acceptor (CTxB-AF 647). Lifetime decreased with the addition of the acceptor. The FRET efficiency was calculated using the FRET trajectory (in red), showing that most of the lifetime species are positioned under a cursor with an average FRET efficiency of 0.11. (**D**) Time course of the increase of the FRET efficiency after

applying 50 μM SDS. (**E**) Time course of the increase of the FRET efficiency after applying 30 μM Triton X-100. (**F**) Summary of the effects produced by the acute application 5 mM β-cyclodextrin, 1 mg/ml WSC, SDS and Triton X-100 as shown in the panel D and E. Data shown are mean ± s.e.m., n = 4 – 16, *$p < 0.05$; **$p < 0.01$.

To conduct live-cell time-resolved FRET imaging, we used a confocal scanning FLIM system to measure FRET efficiency (also see the methods). First, we employed only CTxB AF-488 conjugates, serving as the FRET donor, at a concentration of 20 nM, supplemented in the cell culture medium, to label the plasma membrane of tsA-201 cells — a modified version of human embryonic kidney (HEK) cells. By using a pulsed laser for excitation, the frequency-domain lifetime information corresponding to each image pixel in the intensity-based image was transformed into a pixel on a Cartesian coordinate system, known as “phasor plot”, which exhibits a semicircular shape (Fig. 1B and Supplementary Fig. 1A) (37). This semicircle serves as a reference for pure single-exponential lifetimes, while multiexponential lifetimes are observed within the boundaries of the semicircle. Notably, shorter lifetimes demonstrate a clockwise movement along the semicircle. The phasor approach offers several advantages, including unbiased measurement of fluorescence lifetimes without the necessity of exponential fitting, and the capability to map multiple cursors to identify distinct lifetime species within confocal images (37-40).

When both FRET donors (CTxB AF-488) and acceptors (CTxB AF-647) were present at a concentration of 20 nM, the lifetime characteristics observed in labeled tsA cells exhibited a clockwise shift towards shorter lifetimes, indicating the occurrence of FRET (Fig. 1C). To calculate the FRET efficiency, we used the FRET trajectory method enabled by the phasor plot. The FRET trajectory begins at a zero FRET efficiency position, aligning with the donor-alone cursor, and proceeds through the measured phasor species. Ultimately, it reaches the theoretical 100% FRET efficiency located at the origin coordinate (0, 0). At this point, the background noise primarily consists of white noise with an infinite lifetime contribution. Moreover, the FRET efficiency for each pixel was determined using the FRET trajectory function, generating a heatmap based on FRET efficiency, providing an overview of the FRET distribution of a single cell.

We conducted additional experiments to investigate the impact of the cholesterol-extracting reagent β-cyclodextrin (β-CD) and amphipathic ionic detergents on FLIM-FRET efficiency in tsA-201 cells. Our findings indicate that the acute application of β-CD (5 mM) significantly reduced FRET, while supplementing cholesterols using 1 mg/ml preloaded methyl-β-CD-cholesterol complexes “water soluble cholesterol” (WSC) elevated FRET. In addition, the treatment of ionic detergents, such as

sodium dodecyl sulfate (SDS) and Triton X-100, at micromolar concentrations increased FRET levels (Fig. 1 D-F). These results suggest that the extraction of cholesterol leads to the separation of OMDs, the addition of cholesterol expands OMDs, whereas low concentrations of detergents (50 μM SDS or 30 μM Triton X-100) promote the merging of OMDs. We also employed β-CD on Xenopus oocyte membranes and obtained similar reduction of the FRET as seen in tsA cells (Supplementary Fig. 1B). Previous research has demonstrated that application of amphipathic detergents triggers clathrin-independent massive endocytosis (MEND) during the application of Triton X-100 or after the application of SDS (3, 41). MEND was demonstrated to be able to internalize a substantial portion of the plasma membrane (3, 41, 42). Our results lend new support to the notion that detergent-induced MEND involves the coalescence of OMDs.

Domain size of OMDs varies depending on the cell type

Using FLIM-FRET and CTxB Alexa Fluor 488 or 647 conjugates, we conducted measurements to determine FRET efficiency indicative of OMD size in various primary cells and cultured cell lines (Fig. 2). These included isolated rat dorsal root ganglion (DRG) somatosensory neurons, isolated mouse primary hepatocytes, isolated mouse dermal fibroblasts, isolated mouse cardiac pacemaker cells, embryonic cultured rat cardiomyocytes (H9c2 cells), and tsA cells. Importantly, significant differences were observed between the different cell types, with pacemaker cells demonstrating the highest FRET levels (Fig. 2 A-D), thereby documenting substantial heterogeneity in the size of lipid domains in the plasma membrane of different cell types.

DRG neurons, which are pseudo-unipolar sensory neurons, play a crucial role in transmitting sensory information from the periphery to the spinal cord, particularly for pain sensation (43, 44). DRG neurons that have a relatively small-diameter and mostly unmyelinated axons (C-fibers) are responsible for relaying nociceptive, thermal, and mechanoreceptive signals. Conversely, large-diameter DRG neurons, which are non-nociceptive, mostly transmit mechanoreceptive and proprioceptive signals through large-diameter myelinated axons (44). Impressively, the FRET efficiency in the smaller neurons with cell capacitance less than ~28 pF was found to be significantly greater than in neurons of larger size. This result suggests that heterogeneity in the OMD size of sensory neurons could potentially affect or regulate the excitability of these neurons.

Figure 2

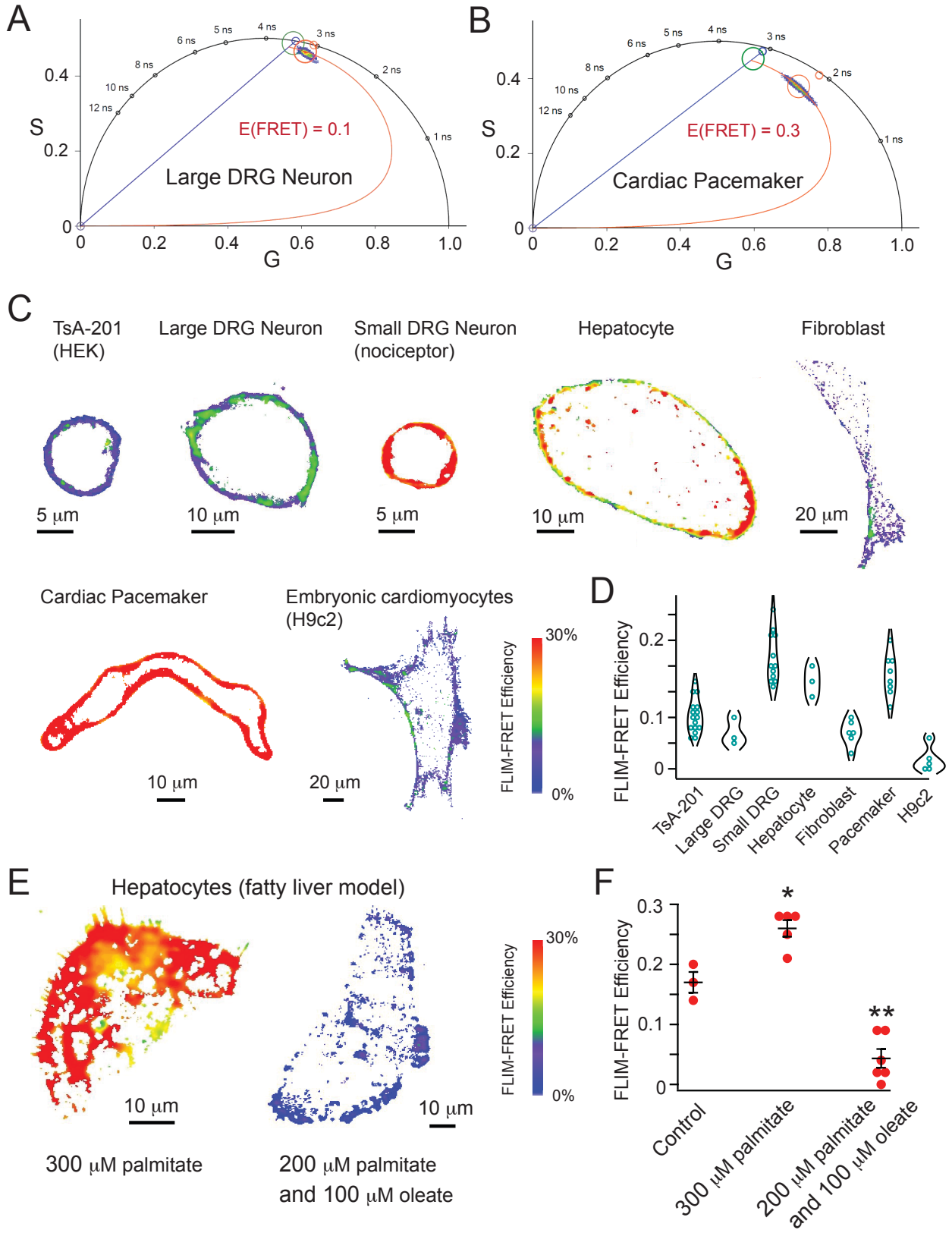
A
S
G
E(FRET) = 0.1
Large DRG Neuron
B
E(FRET) = 0.3
Cardiac Pacemaker
C
TsA-201 (HEK)
Large DRG Neuron
Small DRG Neuron (nociceptor)
Hepatocyte
Fibroblast
Cardiac Pacemaker
Embryonic cardiomyocytes (H9c2)
FLIM-FRET Efficiency
30%
0%
D
TsA-201
Large DRG
Small DRG
Hepatocyte
Fibroblast
Pacemaker
H9c2
E
Hepatocytes (fatty liver model)
300 μM palmitate
200 μM palmitate and 100 μM oleate
F
Control
300 μM palmitate
200 μM palmitate and 100 μM oleate

Figure 2. FLIM-FRET reports the OMD abundance in different cell types.
(**A**) Representative phasor plot of a large DRG neuron showing the CTxB-AF 488/CTxB-AF 647 FLIM-FRET. Using the FRET trajectory, the average FRET efficiency is estimated at 0.1. (**B**) Representative phasor plot of a cardiac pacemaker cell. Using the same FRET pair and FRET trajectory method, the average FRET efficiency of this cell is estimated at 0.3. (**C**) Representative single-cell heatmap images of the localized FLIM-FRET efficiencies of different cell types as illustrated. (**D**) Summary data of the FRET efficiencies of different cell types tested in the panel c. n = 3 - 16 (**E**) Representative heatmap images of mouse hepatocytes with different fatty acid treatments. (**F**) Summary data of the effects produced by the palmitate supplementation versus the combination of palmitate and oleate supplementations as shown in the panel E. Data shown are mean ± s.e.m., n = 3 – 6, *p < 0.05; **p < 0.01.

Lipid tail structure influences the OMD size: an *in vitro* fatty liver model

The formation of OMDs relies on the tight packing of sphingolipids with saturated lipid tails and cholesterols. To investigate the impact of supplementing fatty acids such as palmitate and oleate on the FRET between CTxB-conjugated Alexa Fluor 488 and 647, we implemented protocols commonly used to generate *in vitro* models of fatty liver disease. For hepatocytes, the overnight treatment of additional 300 μM palmitate in the culture medium in the presence of albumin, resulted in a significant increase in FRET efficiency (Fig. 2 E and F). However, combining 200 μM palmitate with 100 μM oleate nearly abolished the FRET signal, indicating a division of the OMDs (Fig. 2 E and F).

In this cell model of fatty liver, the addition of palmitate induces cellular stress on the cells, potentially leading to lipotoxicity (45, 46). Conversely, the inclusion of oleate can act as a preventive measure against such cellular stress (45). Notably, oleate is a monounsaturated fatty acid (18:1) with a double bond that induces a tilt and increased flexibility in the carbon chain, in contrast to the saturated aliphatic chain (16:0) of palmitate. We propose that introducing the tilted aliphatic chain to the lipid membrane greatly impedes the formation of OMDs. These results suggest that the lipotoxicity introduced by palmitates could be partially caused by a substantial increase in the abundance of OMDs, and oleate supplementation can rescue this effect. Moreover, these findings further validate the reliability of our approach using CTxB-conjugated Alexa Fluor 488 and 647~~,~~ in assessing the size and abundance of OMDs.

Disrupting OMDs accelerates action potential firing of nociceptor DRG neurons.

Following the validation experiments using FLIM-FRET to measure OMDs in various cell types, we shifted our focus to DRG sensory neurons. To investigate the potential effects of disrupting OMDs on the firing behavior of small nociceptor DRG neurons, we conducted whole-cell current clamp experiments. We tested whether altering the size of these domains has an impact on the generation of action potentials. To achieve this, we used an acute application (30-60 sec) of β-CD (5 mM) to disrupt OMDs, as confirmed by the observed reduction in FRET efficiency following its application (Fig 3 A and B).

We found that the β-CD treatment led to an increase in the spontaneous action potential firing activity of nociceptor DRG neurons (Fig. 3 C and D). In our cell culture, nerve growth factor (NGF) was supplemented, which promoted the spontaneous firing of DRG neurons (47), mimicking a pain condition. Furthermore, with positive current injections, the action potential firing frequency increased as expected. Cells treated with β-CD also showed more frequent current injection-elicited firing than control cells (Supplementary Fig. 2). The observed augmentation in the spontaneous and the elicited firings of these DRG neurons by the disruption of OMDs suggests that these neurons exhibit a state of increasing hyperactivity. This finding is consistent with a pain phenotype, suggesting that the alteration of OMDs contributes to the modulation of neuronal excitability during the development of chronic pain. We also tested the addition of cholesterol using acute 1 mg/ml WSC treatment. In the presence of NGF, the percentage of spontaneous firing reduced from 50% for the control to 30% after the WSC treatment. The ability of nociceptor DRG neurons to fire action potential with positive current injection was also compromised after the WSC treatment (Supplementary Fig. 2). These results suggest that expanding the OMD by cholesterol enrichment could be used to rescue membrane hyperexcitability and alleviate pain.

Figure 3

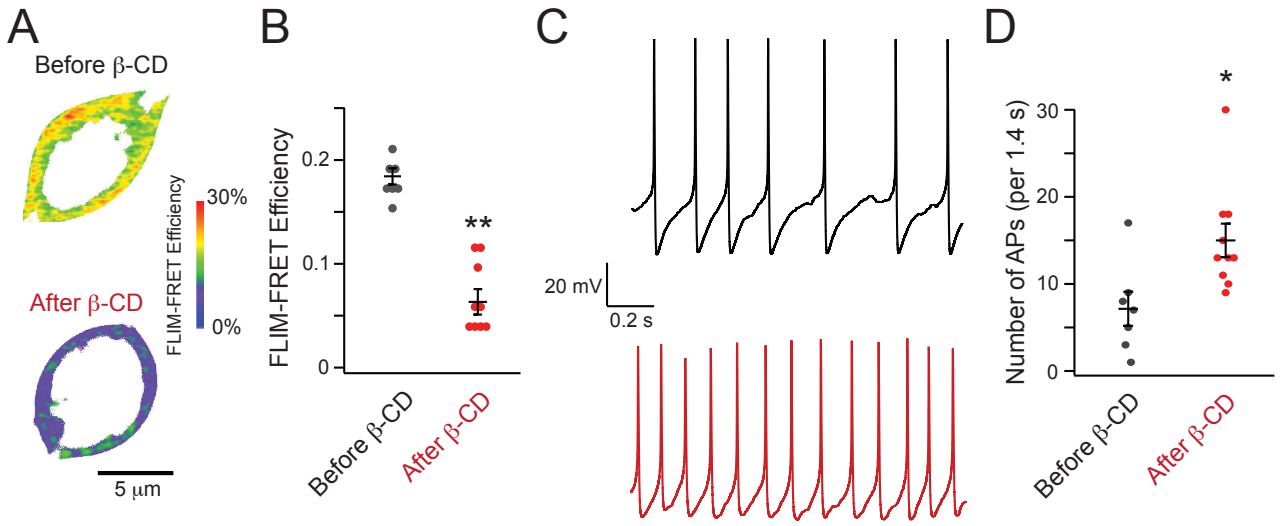

Figure 3. Disrupting the OMD accelerates the action potential firing of DRG neurons.
(**A**) Representative heatmap FRET images of small nociceptor DRG neurons before and after the acute β-cyclodextrin treatment. (**B**) Summary data of the effect of β-cyclodextrin on the FRET efficiency calculated using the phasor plot of small DRG neurons as done in the panel A. Data shown are mean ± s.e.m., n = 7 – 9. (**C**) Representative spontaneous action potential firings of small DRG neurons before and after the acute β-cyclodextrin treatment. (**D**) Summary data of the effect of β-cyclodextrin on number of the spontaneous action potential firing during the 1.4 second recording period. Data shown are mean ± s.e.m., n = 7 – 10, *p < 0.05; **p < 0.01.

Paclitaxel, a drug that produces chemotherapy-induced neuropathy, disrupts OMDs

Chemotherapy-induced peripheral neuropathy (CIPN) affects approximately 40% of chemotherapy patients and lacks effective treatments at present (48). Paclitaxel (Taxol), a widely used chemotherapeutic agent, is known to induce both acute and chronic CIPN. Considering the role of OMD in regulating voltage-gated ion channels and the previously reported role of paclitaxel in regulating membrane lipid domains (12, 28, 49, 50), we postulated that the neuropathy triggered by paclitaxel might be associated with alterations in the lipid domain organization of nociceptor DRG neurons. Using the FLIM-FRET and the same CTxB-mediated labeling approach, our results revealed that overnight treatment using either a low concentration (10 nM) or a saturating concentration (1 μM) of paclitaxel resulted in a significant reduction in the FLIM-FRET efficiency of small DRG neurons (Fig. 4 A-D). In contrast, the same treatment of paclitaxel did not produce a considerable reduction in the FLIM-FRET efficiency of large DRG neurons, which could be because the size and the abundance of OMD in large

DRG neurons is already low (Fig. 4D). In addition, consistent with the results seen with the β-CD treatment, the action potential firing of nociceptor DRG neurons was accelerated after the treatment of 10 nM paclitaxel (Fig. 4 E and F). This finding supports our hypothesis, suggesting that the disruption of OMDs underlies the paclitaxel-induced neuropathy. Since paclitaxel targets tubulin and microtubules, this finding also suggests a dependence of OMDs on the cellular cytoskeleton.

Figure 4

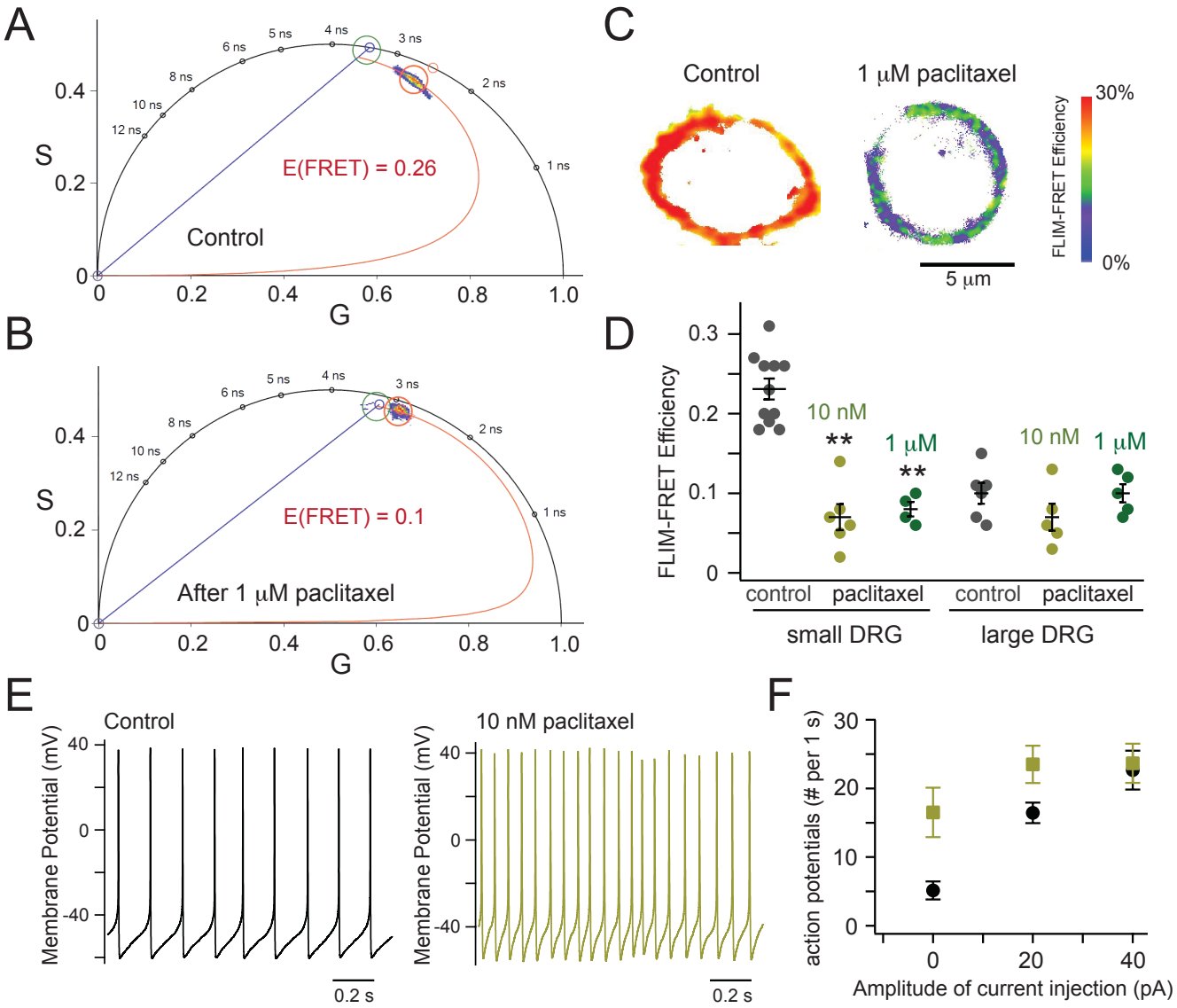

Figure 4. Effects of the CIPN-related drug paclitaxel on DRG neurons.

(**A-B**) Representative phasor plot of a small nociceptor DRG neuron before and after the overnight 1 μM paclitaxel treatment, using the CTxB-AF 488/CTxB-AF 647 FLIM-FRET. (**C**) Representative heatmap FRET images of small

nociceptor DRG neurons before and after the paclitaxel treatment. (**D**) Summary of the effect on FRET efficiencies of small and large DRG neurons caused by the paclitaxel treatments as in the panels A-C. Data shown are mean ± s.e.m., n = 4 – 6, *p < 0.05; **p < 0.01. (**E**) Representative spontaneous action potential firings of small DRG neurons before and after the overnight 10 nM paclitaxel treatment. (**F**) Summary results of the number of action potentials plotted against of the amplitude of current injection. Data shown as mean ± s.e.m.

Facilitated native HCN currents of nociceptor DRG neurons after disrupting OMDs

A key player in regulating the electrical excitability of DRG neurons is the pacemaker hyperpolarization-activated HCN channels (16, 20). With physiological electrochemical driving force, they conduct inward currents primarily carried by sodium ions, which depolarize the membrane potential, bringing it closer to the threshold of firing action potential. The native HCN channel currents of small nociceptor DRG neurons were elicited by a series of hyperpolarizing voltages using whole-cell voltage clamp, exhibiting a conductance-voltage (G-V) relationship with a voltage for the half maximal activation ($V_{1/2}$) of -94 mV, close to that of HCN2 channels (Fig. 5 A, C, D) (16, 20). Addition of a saturating concentration of cyclic adenosine monophosphate (cAMP, 0.5 mM) in the pipette solution shifted the G-V relationship to more depolarized voltages, with a $V_{1/2}$ of -84 mV (Fig. 5 B, C, D). In comparison, large DRG neurons primarily express the HCN1 isoform, which is not particularly sensitive to cAMP (20).

We found that disrupting OMDs using the same acute application of β-CD altered the hyperpolarization-dependent activation of endogenous HCN channels of small nociceptor DRG neurons. In the absence of cAMP supplementation, β-CD treatment did not shift the $V_{1/2}$, but instead increased the slope factor of the G-V relationship according to the Boltzmann sigmoidal fit, suggesting less gating charge movement during the channel activation (Fig. 5, C-E). The estimated number of charge movement for the channel activation was 2.83 ± 0.07 for the control and 2.48 ± 0.1 after the β-CD treatment ($p < 0.05$). Furthermore, with 0.5 mM cAMP in the pipette solution, β-CD treatment also failed to further shift the $V_{1/2}$ for the channel activation to more depolarized voltages. Nevertheless, the slope factor associated with the Boltzmann fit of the G-V relationship increased significantly, suggesting that in the presence of cAMP, the estimated gating charge movement across the membrane was decreased (Fig. 5, C-E). With cAMP, the calculated number of charge movement for the channel activation was 2.98 ± 0.8 for the control and 2.41 ± 0.2 after the β-CD treatment ($p < 0.05$). This change of the effective gating charge movement could be related to the membrane-thinning effect after disrupting the OMD, which might narrow the focused electric field of the membrane. On the other hand,

the shallower slope of the G-V relationship produces a much higher channel open probability at the RMP (around -60 mV). Specifically, the relative open probability of HCN channels increased from 6 ± 1% for the control to 11 ± 2% after the β-CD treatment in the presence of cAMP. This increase in open probability of HCN channels near the RMP could effectively depolarize the membrane to promote action potential firing. In addition, using the obtained parameters from the Boltzmann fits, the free energy (ΔG) associated with the HCN channel activation can be calculated. It is evident that a lower amount of free energy was required to open the channel after the β-CD treatment, regardless of the presence or absence of cAMP (Fig. 5F). This observation suggests that the disruption of the OMD led to an energetic facilitation of the HCN channel opening process, which is physiologically important at the RMP.

Figure 5

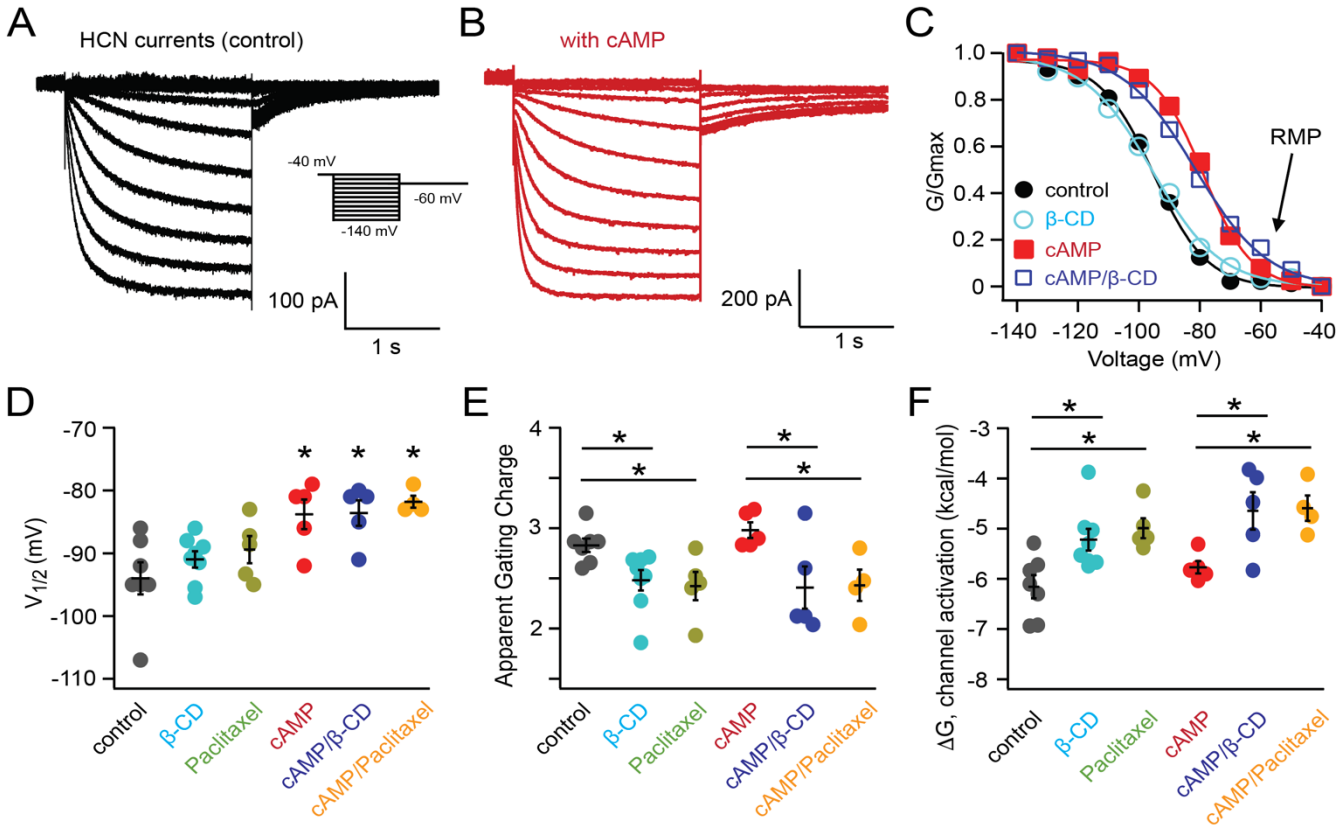

Figure 5. Effects of disrupting OMDs on the native HCN currents of nociceptor DRG neurons. (**A-B**) HCN currents elicited by a series of hyperpolarizing voltage pulses from -40 mV to -140 mV, in the presence (red) or in the absence (black) of 0.5 mM cAMP in the pipette solution. (**C**) Representative conductance-voltage relationships of the endogenous HCN currents in the following conditions: control, with β-cyclodextrin, with cAMP, and with both β-cyclodextrin and cAMP. (**D-F**) Summary of effects of β-cyclodextrin, 10 nM paclitaxel, and cAMP

on the gating parameters of endogenous HCN currents: $V_{1/2}$, estimated gating charge, and the free energy for the channel activation. Data shown are mean ± s.e.m., n = 4 – 8, *p < 0.05; **p < 0.01.

We next evaluated the effect of 10 nM paclitaxel on the gating of HCN channels in small DRG neurons (Fig. 5 D-F). Similar to the influence of β-CD on HCN currents, the HCN G-V relationship after paclitaxel treatment manifested a mostly unchanged $V_{1/2}$, but a significantly shallower slope. With paclitaxel, the measured number of charge movement for the channel activation was 2.42 ± 0.14 in the absence of cAMP and 2.43 ± 0.14 in the presence of 0.5 mM cAMP. The ΔG associated with the HCN channel activation was also decreased considerably after the paclitaxel treatment (Fig. 5F). These findings suggest that the paclitaxel-induced change in HCN channel gating, leading to heightened HCN current near the RMP, could contribute to the hyperexcitability observed in DRG neurons following this type of chemotherapy.

In addition, we tested whether the primary HCN-channel type HCN2 channels expressed in nociceptor DRG neurons are localized in OMDs. Using the phasor FLIM-FRET method and an OMD-specific fluorescent probe L10-CFP, we found considerable FRET between the L10-CFP and a human HCN2-YFP construct expressed in tsA 201 cells (Supplementary Fig. 3). The L10 probe, validated by our earlier work, is derived from the first 10 amino acids located at the amino terminus of Lck kinase (28, 51). L10-CFP localizes to OMDs specifically, and was shown to have low FRET with human HCN1-YFP but exhibit higher FRET with the human HCN4-YFP (28). Here, with live-cell imaging, we found that, similar to HCN4, human HCN2 channels also had a tendency to localize to OMDs.

Smaller OMDs of DRG neurons in a nerve injury-induced model of neuropathic pain

Mechanical allodynia and neuropathic pain are known to manifest following peripheral nerve damage. To define the potential correlation between nerve injury-induced neuropathic pain and changes in the size of OMDs, we also used the FLIM-FRET method to assess OMD size in DRG neurons in a spared nerve injury (SNI) model of neuropathic pain (52) (Supplementary Fig. 4). Our study revealed that the FRET efficiency, which reports OMD size, displayed a reduction in both large and small DRG neurons (Fig. 6A). Specifically, the FRET efficiency measured from small DRG neurons decreased from 10.4 ± 1.8% for the control neurons on the contralateral side of the injury to 4.3 ± 0.5% for the neurons on the ipsilateral side of the injury. And for large DRG neurons, the FRET changed from 2.5 ± 1.0% for the contralateral ones to 1 ± 0.6% for the ipsilateral ones. These results suggest that downsizing the OMD is not only observed in the *in vitro* paclitaxel-induced neuropathy model but also in

the *in vivo* nerve injury-induced pain model, implying that it is a general phenomenon associated with neuropathic pain (Fig. 6B). In other words, the size of OMDs could potentially serve as an indicator of neuropathic pain. The punch line is that membrane compartmentalization and lipid domain-domain separation, controlled by cholesterols, regulate the voltage sensing of ion channels and excitability of cell membranes.

Figure 6

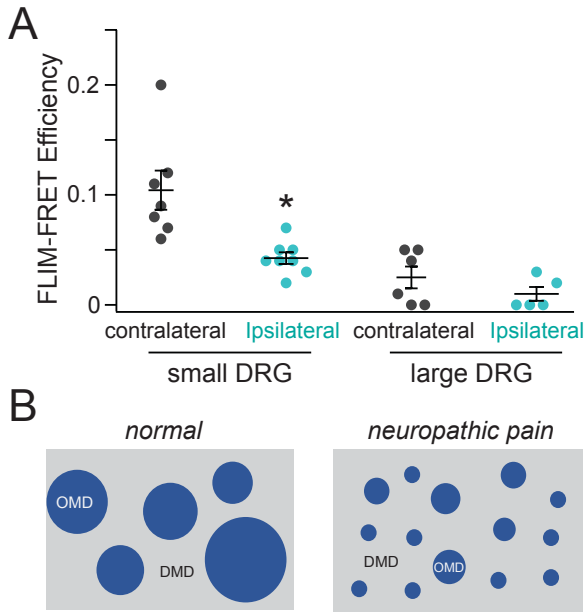

Figure 6. Effects on the OMD size of DRG neurons in a spared nerve injury model of neuropathic pain. (**A**) Summary of the effect on the FRET efficiencies of small and large DRG neurons in the pain model. Data shown are mean ± s.e.m., n = 5 – 8, *p < 0.05; **p < 0.01. (**B**) Cartoon illustrating the concept that downsizing the OMD serving as an indicator of neuropathic pain.

Discussion

Neuropathic pain (53, 54), a prevalent and debilitating condition, arises from nerve injury, infections, diabetes, and frequently, "channelopathies." Despite its widespread occurrence, effective treatments for neuropathic pain are currently lacking. To manage severe neuropathic pain, opioids are commonly prescribed; however, their use carries the risk of addiction or overdose (53, 55). Recently, pacemaker HCN channels have emerged as promising therapeutic targets for addressing neuropathic pain (21, 56, 57). This current study not only enhances our understanding of HCN channels, but also provides insights into potential strategies to combat neuropathic pain. Additionally, we investigated a previously overlooked aspect for the pain research: how membrane compartmentalization, particularly OMDs, influences ion channels (3). Considering the emerging roles of OMDs in cardiovascular disorders, viral infections, Alzheimer's disease, and inflammation, this research holds significant implications for multiple fields in physiology.

During the course of evolution, some cells, particularly neurons, developed the ability to carry out rapid, repetitive action potential firing. Presumably, this ability required a host of biochemical and biophysical adaptations. Our research suggests that electrically active cell membranes may require abundant OMDs as a protective and adaptive mechanism to maintain a stable membrane structure that supports or accommodates repetitive action potential firing. In this study, we observed that small nociceptive DRG neurons possess larger OMDs than large DRG neurons. This finding is consistent with the idea that a low percentage (~15%) of large DRG neurons display spontaneous firing, under our experimental condition in the presence of NGF in the culture medium. On the other hand, a significant percentage (~50%) of small DRG neurons exhibit spontaneous firing. This correlation supports the idea that OMDs play a role in adapting to the electrical demands of the cell. Our hypothesis gains further support from the data collected from five other types of cells tested. For instance, cardiac pacemaker cells, which fire rhythmic action potentials, display the largest OMD size among all the non-neuronal cell types examined in this study. Hepatocytes, known for their cholesterol synthesis, also possess relatively large OMDs. Conversely, fibroblasts, embryonic kidney cells, and cultured H9c2 cardiomyocytes were found to have relatively small OMDs. In conclusion, our findings present a previously unexplored concept that the lipid composition and the compartmentalization of the cell membrane adapt in response to the specific electrical requirements of the cell. This concept sheds light on the mechanisms underlying cellular adaptation during evolution and may have implications for understanding various neuronal and cardiac diseases.

Our study establishes novel connections between the pacemaker HCN channel, membrane compartmentalization, and neuropathic pain. We speculate that neurotrophic factors and cytokines released from injured peripheral nerves or during paclitaxel treatment could lead to altered cell signaling and decreased OMD size. This, in turn, affects the trafficking and localization as well as the function of ion channels including voltage-gated sodium channels, as previously observed (50, 58). Here, our findings demonstrate that disrupting OMDs makes HCN channels more conductive and sensitive to voltage. In a separate study, we showed that the integrity of the OMD plays a crucial role in the rearrangement of voltage sensors (28). We believe that the movement of the unusually long S4-helix of HCN channels is highly sensitive to the “hydrophobic (mis)match” with the lipid bilayer's hydrophobic region. Considering that this hydrophobic mismatch often plays a critical role in influencing the tilt angle of transmembrane helices (59, 60), we hypothesize that re-localizing HCN channels from OMDs to DMDs increases the tilt angle of the S4 helix. This phenomenon can be attributed to the difference in lipid bilayer thickness comparing OMDs with DMDs (5). Consequently, this increase in the

tilting motion of the S4 helix facilitates pore domain activation through its interaction with the channel pore domain (61). Interestingly, disrupting OMDs leads to reduced charge movement across the electric field of HCN channels, consistent with an alteration in voltage-sensor movement of HCN channels, or alternatively, suggesting a more focused electric field of the membrane. Similar changes of the gating charge movement could happen for other types of voltage-gated ion channels when OMDs are disrupted. Our observations support the notion that changes in OMDs have significant implications for ion channel function and could lead to the development of neuropathic pain.

Materials and Methods

Molecular biology, cell culture and transfection

The human HCN2 cDNA was synthesized by VectorBuilder (Chicago, IL). The construct was amplified using a mammalian gene expression vector containing a carboxyl-terminal YFP and a CMV promoter. The L10-CFP was a gift from Bertil Hille (University of Washington, Seattle, WA). DNA concentration was measured using a Nanodrop OneC spectrophotometer (Life Technologies, Grand Island, NY).

The tsA-201 cells (a variant of human embryonic kidney HEK cells) were obtained from Sigma-Aldrich (St. Louis, MO). Cells were cultured in Dulbecco's modified Eagle's medium (DMEM; Gibco) supplemented with 10% fetal bovine serum (FBS; Gibco) and 1% penicillin/streptomycin (Gibco) in a humidified incubator at 37°C with 5% CO_2 in tissue culture dishes (CellTreat, Pepperell, MA). Transfection was performed on 70%-90% confluent tsA-201 cells using the lipofectamine 3000 Kit (Invitrogen, Carlsbad, CA, #L30000080), following previously established protocols (51, 62).

The Cholera Toxin Subunit B-Alexa Fluor™ 488 and 647 conjugates were obtained from Thermo Fisher Scientific and applied to cultured cells at a concentration of 20 nM for a duration of ~10 minutes. The binding affinity of CTxB to GM1-enriched membrane falls within the picomolar range (33).

Isolated oocytes were purchased from EcoCyte (Austin, TX) and cultured in a saline-like solution ND96 (96 mM NaCl) supplemented with antibiotics (100 U/ml penicillin/100 μg/ml streptomycin).

Fluorescence Lifetime measurement and FLIM-FRET

A Q2 laser scanning confocal system, equipped with a FastFLIM data acquisition module from ISS, Inc. (Champaign, IL), and two hybrid PMT detectors (Model R10467-40, Hamamatsu USA, Bridgewater, NJ), was used for digital frequency-domain fluorescence lifetime imaging as previously done (28, 63). This confocal FLIM system was connected to an Olympus IX73 inverted microscope (Olympus America, Waltham, MA). The fluorescence lifetime measurements provided both frequency-domain (instantaneous distortion-free phasor plotting) and time-domain decay information. Confocal imaging was made possible using dichroic cubes, one with a 50/50 beam splitter and the other equipped with various long-pass filters. A supercontinuum laser (YSL Photonics, Wuhan, China) was

used for fluorescence excitation, with a wavelength range of 410 nm to 900 nm, a repetition rate of 20 MHz, and a pulse duration of 6 ps. Specifically, the excitation wavelengths were 445 nm for CFP, 488 nm for AF-488 and YFP. The intensity of laser excitation was kept at the same level when imaging different cell samples. To detect the emission from the CFP/YFP FRET pair, an emission filter cube comprising a 475/28 nm filter for CFP, a 495 nm long-pass dichroic mirror, and a 542/27 nm filter for YFP was used. A 525/40 nm emission filter was used for detecting the AF-488 emission. For phasor FLIM-FRET, only the donor lifetime was measured either in the absence or in the presence of the FRET acceptor.

Under each experimental condition, confocal images with a frame size of 256 x 256 pixels were acquired. A motorized variable pinhole with a size of 100 μm and a pixel dwell time ranging from 0.1 to 0.4 ms were used during image acquisition. For image processing, display, and acquisition, the VistaVision software (ISS, Inc., Champaign, IL) was used. This software allows for the customization of parameters such as pixel dwell time, image size, and resolution. The FLIM analysis used a fitting algorithm, phasor plotting and analysis. To enhance the display and analysis of membrane-localized lifetime species, a median/gaussian smoothing filter and an intensity-threshold filter were applied.

The VistaVision software was used to determine the phase delays (φ) and modulation ratios (m) of the fluorescence signal in response to an oscillatory stimulus with frequency ω. These values were derived by conducting sine and cosine Fourier transforms of the phase histogram, considering the instrument response function (IRF) calibrated with different fluorophores with known lifetimes in water. The choice of calibration fluorophore (Atto 425, rhodamine 110, or rhodamine B) depended on the emission spectrum of the fluorophore of interest, with respective lifetimes of 3.6 ns, 4 ns, and 1.68 ns.

The FLIM-FRET analysis was performed using the FRET trajectory function available in the VistaVision software (37). To ensure accurate results, three crucial parameters were adjusted to optimize the fitting trajectory, encompassing both the unquenched donor and the donor species affected by FRET. These parameters included: the background contribution in the donor sample, the unquenched donor contribution in the FRET sample, and the background contribution in the FRET sample. To maintain accuracy, the background levels in both the donor sample and the FRET samples were set below 4%. This value corresponds to the very low emission intensity typically observed in unlabeled cells.

Patch-clamp Electrophysiology

The whole-cell patch-clamp recordings were performed using an EPC10 patch-clamp amplifier and PATCHMASTER (HEKA) software, with a sampling rate of 10 kHz. Borosilicate patch electrodes were created using a P1000 micropipette puller from Sutter Instrument (Sutter, Novato, CA), resulting in an initial pipette resistance of approximately 3 - 5 MΩ. A Sutter MP-225A motorized micromanipulator was used for patch clamp (Sutter, Novato, CA). The recordings were conducted at a temperature range of 22-24 °C.

To record HCN currents from DRG neurons, the internal pipette solution was prepared with the following composition (in mM): 10 NaCl, 137 KCl, 1 $MgCl_2$, 10 HEPES, 1 EGTA, and pH 7.3 adjusted with KOH. In addition, 0.5 mM cAMP was added to the internal solution to facilitate the endogenous HCN currents. The external solution used was prepared with the following composition (in mM): 154 NaCl, 5.6 KCl, 1 $MgCl_2$, 1 $CaCl_2$, 8 HEPES, 10 D-Glucose, and pH 7.4 adjusted with NaOH. Series resistance was typically lower than 15 MΩ and series resistance compensation was set at 40%. For the action potential measurements, current clamp mode of PATCHMASTER was employed instead of the whole-cell voltage-clamp configuration.

The conductance-voltage (G-V) relationships of endogenous HCN currents were measured from the instantaneous tail currents at -60 mV following voltage pulses from -40 mV to between 0 and −140 mV. The leak tail currents following pulses to -60 mV were subtracted, and the currents were normalized to the maximum tail current amplitude, reporting the relative channel conductance (G/G_{max}). The relative conductance was plotted as a function of the voltage of the main pulse and fitted with the Boltzmann equation:

$$G/G_{max}=1/(1+exp[(V-V_{1/2})/Vs]) \qquad (11)$$

where V is the membrane potential, $V_{1/2}$ is the potential for half-maximal activation, and Vs is the slope factor. Vs = RT/zeF, where R is the gas constant, T is temperature in Kelvin (297 K), F is the Faraday constant, *e* is the value of elementary charge, z is the estimated number of elementary gating charge per channel for channel activation. The Gibbs free energy needed for channel activation was calculated according to: $\Delta G = RTV_{1/2}/Vs$ (64).

Mouse Studies

All experiments involving the isolation of primary cells from mice were conducted in accordance with the guidelines approved by the Institutional Animal Care and Use Committee (IACUC) of Saint Louis University, adhering to the best practices outlined in the Guide for the Care and Use of Laboratory Animals. The mice used in the study were of the wild-type C57BL/6J strain and were bred from an in-house colony. The mice were housed in a specific-pathogen-free animal facility at Saint Louis University, where they were subjected to a 12-hour light/dark cycle and provided with controlled normal temperature and humidity levels. Throughout the study, the mice had *ad libitum* access to normal chow and water. For primary cell isolation, male or female mice aged between 10 to 20 weeks were used.

Primary Hepatocyte Isolation and Culture

Primary murine hepatocytes were isolated following a two-step perfusion method, as previously described (65). Mice were euthanized using deep isoflurane anesthesia followed by cervical dislocation. The abdominal cavity was promptly exposed, and a 22-gauge intravenous catheter was cannulated into the portal vein. The liver was initially perfused with Hank's buffered salt solution (HBSS, Gibco) supplemented with 0.5 mM EGTA at a flow rate of 5 mL/min to clear blood from the hepatic vasculature. Simultaneously, an incision was made in the inferior vena cava to drain the perfusate and prevent over-pressurization. After 4-5 minutes of HBSS perfusion, the pump tubing was switched to perfuse serum-free Dulbecco's modified eagle's medium (DMEM; Sigma) containing 1 mg/mL type IV collagenase (Sigma). The collagenase perfusion lasted for another 4-5 minutes, allowing for liver digestion. Both the HBSS and collagenase solutions were warmed to 37°C before and during perfusion. Following the removal of the gallbladder, the digested liver was transferred to a 10-cm petri dish containing 10 mL of collagenase-DMEM solution, and the capsule layer was manually removed using forceps. The digested liver lobes were then dispersed by pipetting up and down with a 25 mL serological pipette. The cell suspension was supplemented with 15 mL of ice-cold 10% FBS-DMEM, passed through a 100 μm cell strainer, and kept on ice. Cells were pelleted at 0.5 x g for 2 minutes, washed with fresh 10% FBS-DMEM, recentrifuged, and suspended again in fresh 10% FBS-DMEM. Cell counting was performed using a hemocytometer, and the cells were plated on type-I collagen-coated glass-bottomed dishes at a concentration of 200,000 cells/mL in 10% FBS-DMEM supplemented with penicillin/streptomycin and amphotericin B. The cells were allowed to adhere to the dishes for 3-4 hours before being cultured overnight in basal DMEM (glucose, serum, and phenol-red free; Sigma) supplemented with either 300 μM BSA-palmitate, 200 μM BSA-palmitate plus 100 μM BSA-oleate, or equimolar fatty-acid free BSA

(BSA-conjugated fatty acids from Cayman Chemical; 6:1 fatty acid to BSA ratio) in a 5% CO_2 incubator at 37°C. Imaging of the cells was performed the following day.

Dermal Fibroblast Isolation and Culture

Adult murine dermal fibroblasts were isolated from the ear lobes of mice using a humane method involving deep isoflurane anesthesia followed by cervical dislocation. The ear tissue was minced with a razor blade and placed into wells of a 6-well plate. It was then digested overnight in a 5% CO_2 incubator at 37°C using 500 units of collagenase in 20% FBS-DMEM supplemented with penicillin/streptomycin. The following day, the cells were dispersed by pipetting up and down with a 5 mL pipette. The cell suspension was transferred into a 15 mL conical tube, centrifuged at 1500 rpm for 5 minutes, and the cell pellet was resuspended in 5 mL of fresh 20% FBS-DMEM. The cells were then plated onto a 6-cm dish. Once the fibroblasts reached confluency, they were passaged by trypsinization. For imaging purposes, cells at passages 2-3 were used, and they were seeded onto glass-bottomed dishes at a concentration of 100,000 cells/mL.

H9c2 Cell Culture

H9c2 embryonic rat cardiomyocyte cells were obtained from the American Type Culture Collection (ATCC, Manassas, Virginia) and cultured in 10% FBS-DMEM until ~90% confluent before passaging by trypsinization. Cells were used at passages 3-10. Cells were plated on glass-bottomed dishes at 100,000 cells/mL for imaging.

Isolation of murine pacemaker cells

The isolation and culturing of mouse pacemaker cells was refined from the procedures outlined in a previous paper (66). In summary, wild-type C57BL/6J mice were anesthetized by isoflurane, thoracotomy performed, and the beating hearts surgically harvested. The heart explant was rapidly immersed in warm Tyrode's solution (pH 7.4) with the following composition (in mM): 140 NaCl, 5.4 KCl, 1 $MgCl_2$, 1.8 $CaCl_2$, 5 HEPES, and 5.5 glucose. The sinoatrial node (SAN) was identified under a dissection microscope and carefully excised from the superior vena cava, sulcus terminalis, sulcus coronarius, and inferior vena cava. The SAN was then transferred to a 2-mL reaction tube containing 675 µl of pre-warmed Tyrode's Low-Ca^{2+} solution (pH 6.9) with the following composition (in mM): 140 NaCl, 5.4 KCl, 0.5 $MgCl_2$, 0.2 $CaCl_2$, 5 HEPES, 5.5 glucose, 1.2 KH_2PO_4, and 50 taurine. After a 5-

minute incubation, enzymatic digestion of the SAN was initiated by adding 10 µl of BSA (1 mg/ml), 40 µl of elastase (18.87 U/mg), 125 µl of protease (1.79 U/mg), and 150 µl of collagenase B (0.54 U/mg) to the 2-mL reaction tube. The digestion process occurred for 30 minutes in a 37°C water bath, with additional mechanical dissociation performed every 10 minutes. The reaction was stopped by centrifugation at 200 x g for 2 minutes at 4°C, and the supernatant was discarded. The SAN was then washed three times with 1 mL of ice-cold, calcium-free Kraft-Brühe (KB) solution (pH 7.4) with the following composition (in mM): 80 L-glutamic acid, 25 KCl, 3 $MgCl^{2+}$, 10 KH_2PO_4, 20 taurine, 10 HEPES, 10 glucose, and 0.5 EGTA.

After the washing steps, the SAN tissue was allowed to rest in 350 µl of cold KB solution at 4°C for up to 3 hours. Following the recovery period, the SAN was incubated in a water bath at 37°C for 10 minutes. The SAN cells were mechanically dissociated using a 1000 µl pipette tip and further dissociated with a 200 µl pipette tip. 50 µl of dissociated cells were plated on poly-L-lysine-coated 25 mm coverslips within a 100mm x 15mm petri dish containing moistened paper towels to maintain humidity. The cells were allowed to attach to the coverslip. Before proceeding with experimentation, the cells were returned to physiological conditions, and their automaticity was restored by gradually reintroducing Ca^{2+}. This was achieved by adding Tyrode's solution (pH 7.4) in small increments (10, 22, 50, and 172 µl) every 3 minutes.

Rat Studies

Adult Sprague-Dawley rats (Pathogen-free female 100 g, male 250 g Envigo, Placentia, CA) were kept in light (12-h light: 12-h dark cycle; lights on at 07:00 h) and temperature (23 ± 3°C) controlled rooms. Standard rodent chow and water were available *ad libitum.* All animal use was conducted in accordance with the National Institutes of Health guidelines, and the study was conducted in strict accordance with recommendations in the guidelines approved by the IACUC of Saint Louis University (Protocol #: 3014). All behavioral experiments were performed by experimenters who were blinded to treatment groups.

Primary dorsal root ganglion neurons

Dorsal root ganglia (DRG) were dissected from 100 g female Sprague-Dawley rats (67-70). In brief, removing dorsal skin and muscle and cutting the vertebral bone processes parallel to the dissection stage exposed DRGs. DRGs were then collected, trimmed at their roots, and digested in 3

mL bicarbonate free, serum free, sterile DMEM (Catalog# 11965, Thermo Fisher Scientific, Waltham, MA) solution containing neutral protease (3.125 mg/mL, Catalog# LS02104, Worthington, Lakewood, NJ) and collagenase Type I (5 mg/mL, Cat# LS004194, Worthington, Lakewood, NJ) and incubated for 45 min at 37°C under gentile agitation. Dissociated DRG neurons (~1.5 x 10^6) were then gently centrifuged to collect cells and washed with DRG media DMEM containing 1% penicillin/streptomycin sulfate from 10 000 µg/mL stock, 30 ng/mL nerve growth factor, and 10% fetal bovine serum. Cells were plated onto poly-D-lysine and laminin-coated glass 12-mm coverslips.

Spared nerve injury (SNI) model of neuropathic pain

Under isoflurane anesthesia (5% induction, 2.0 % maintenance in 2 L/min O_2), skin on the lateral surface of the left hind thigh was incised. The biceps femoris muscle was bluntly dissected to expose the three terminal branches of the sciatic nerve (52). Briefly, the common peroneal and tibial branches were tightly ligated with 4-0 silk suture and axotomized 2.0 mm distal to the ligation. Closure of the incision was made in two layers. The muscle was sutured once with 5-0 absorbable suture; skin was auto-clipped. Animals were allowed to recover for 7 days before any testing.

Statistics and Reproducibility

The data parameters were presented as the mean ± s.e.m. of n independent cells or patches. Statistical significance was determined using the Student's t test for comparing two groups, or a one-way ANOVA followed by Tukey's post hoc test for comparisons with more than two groups, denoted as $*p < 0.05$, $**p < 0.01$ respectively.

Acknowledgements

We thank Samantha Deavila for technical support, Donald W. Hilgemann (University of Texas Southwestern Medical Center) for helpful advice and editing the manuscript, Bertil Hille (University of Washington) for support and sharing DNA constructs, and Joel C. Eissenberg (Saint Louis University) for editing the manuscript. This research is supported by startup funds from the Edward A. Doisy Department of Biochemistry and Molecular Biology, Saint Louis University School of Medicine (to G.D. and K.S.M). A.M. is supported by startup funds from Saint Louis University, SLU Institute for Drug & Biotherapeutic Innovation seed grant, National Institutes of Health NINDS R01NS119263, R01NS119263-04S1 and Department of Defense CPMRP #CP220080P1. Cartoons in figures were created using BioRender.

Author Contributions

G.D. conceptualized the research. G.D., A.M., and K.S.M designed experiments. L. J. H. performed electrophysiology experiments, G.D. and N.L.M., performed fluorescence imaging. N.D. and L.S. performed behavior experiments on rats and prepared neuronal samples. G.D., L. J. H., N.L.M., and N.D. analyzed data. G.D. wrote the paper with insightful inputs from other authors.

Competing Interests

The authors declare no competing interests.

References

1. D. Lingwood, K. Simons, Lipid rafts as a membrane-organizing principle. *Science* **327**, 46-50 (2010).
2. I. Levental, E. Lyman, Regulation of membrane protein structure and function by their lipid nano-environment. *Nat Rev Mol Cell Biol* **24**, 107-122 (2023).
3. D. W. Hilgemann *et al.*, Lipid signaling to membrane proteins: From second messengers to membrane domains and adapter-free endocytosis. *J Gen Physiol* **150**, 211-224 (2018).
4. C. Eggeling *et al.*, Direct observation of the nanoscale dynamics of membrane lipids in a living cell. *Nature* **457**, 1159-1162 (2009).
5. C. E. Cornell, A. Mileant, N. Thakkar, K. K. Lee, S. L. Keller, Direct imaging of liquid domains in membranes by cryo-electron tomography. *Proc Natl Acad Sci U S A* **117**, 19713-19719 (2020).
6. M. A. Pavel, E. N. Petersen, H. Wang, R. A. Lerner, S. B. Hansen, Studies on the mechanism of general anesthesia. *Proc Natl Acad Sci U S A* **117**, 13757-13766 (2020).
7. R. J. Andrew *et al.*, Lack of BACE1 S-palmitoylation reduces amyloid burden and mitigates memory deficits in transgenic mouse models of Alzheimer's disease. *Proc Natl Acad Sci U S A* **114**, E9665-E9674 (2017).
8. J. M. Cordy, I. Hussain, C. Dingwall, N. M. Hooper, A. J. Turner, Exclusively targeting β-secretase to lipid rafts by GPI-anchor addition up-regulates β-site processing of the amyloid precursor protein. *Proc Natl Acad Sci U S A* **100**, 11735-11740 (2003).
9. R. Ehehalt, P. Keller, C. Haass, C. Thiele, K. Simons, Amyloidogenic processing of the Alzheimer β-amyloid precursor protein depends on lipid rafts. *J Cell Biol* **160**, 113-123 (2003).
10. K. Fecchi *et al.*, Coronavirus Interplay With Lipid Rafts and Autophagy Unveils Promising Therapeutic Targets. *Front Microbiol* **11**, 1821 (2020).
11. D. Sviridov, Y. I. Miller, R. A. Ballout, A. T. Remaley, M. Bukrinsky, Targeting Lipid Rafts-A Potential Therapy for COVID-19. *Front Immunol* **11**, 574508 (2020).
12. J. M. Navia-Pelaez *et al.*, AIBP regulates TRPV1 activation in chemotherapy-induced peripheral neuropathy by controlling lipid raft dynamics and proximity to TLR4 in dorsal root ganglion neurons. *Pain* **164**, e274-e285 (2023).

13. M. Amsalem, C. Poilbout, G. Ferracci, P. Delmas, F. Padilla, Membrane cholesterol depletion as a trigger of Nav1.9 channel-mediated inflammatory pain. *EMBO J* **37** (2018).
14. J. M. Navia-Pelaez *et al.*, Normalization of cholesterol metabolism in spinal microglia alleviates neuropathic pain. *J Exp Med* **218** (2021).
15. R. B. Robinson, S. A. Siegelbaum, Hyperpolarization-activated cation currents: from molecules to physiological function. *Annu Rev Physiol* **65**, 453-480 (2003).
16. E. C. Emery, G. T. Young, E. M. Berrocoso, L. Chen, P. A. McNaughton, HCN2 ion channels play a central role in inflammatory and neuropathic pain. *Science* **333**, 1462-1466 (2011).
17. S. R. Chaplan *et al.*, Neuronal hyperpolarization-activated pacemaker channels drive neuropathic pain. *J Neurosci* **23**, 1169-1178 (2003).
18. G. T. Young, E. C. Emery, E. R. Mooney, C. Tsantoulas, P. A. McNaughton, Inflammatory and neuropathic pain are rapidly suppressed by peripheral block of hyperpolarisation-activated cyclic nucleotide-gated ion channels. *Pain* **155**, 1708-1719 (2014).
19. L. Luo *et al.*, Role of peripheral hyperpolarization-activated cyclic nucleotide-modulated channel pacemaker channels in acute and chronic pain models in the rat. *Neuroscience* **144**, 1477-1485 (2007).
20. A. Momin, H. Cadiou, A. Mason, P. A. McNaughton, Role of the hyperpolarization-activated current Ih in somatosensory neurons. *J Physiol* **586**, 5911-5929 (2008).
21. E. C. Emery, G. T. Young, P. A. McNaughton, HCN2 ion channels: an emerging role as the pacemakers of pain. *Trends Pharmacol Sci* **33**, 456-463 (2012).
22. C. Tsantoulas *et al.*, Hyperpolarization-activated cyclic nucleotide-gated 2 (HCN2) ion channels drive pain in mouse models of diabetic neuropathy. *Sci Transl Med* **9**, eaam6072 (2017).
23. A. Barbuti *et al.*, Localization of pacemaker channels in lipid rafts regulates channel kinetics. *Circ Res* **94**, 1325-1331 (2004).
24. A. Barbuti *et al.*, A caveolin-binding domain in the HCN4 channels mediates functional interaction with caveolin proteins. *J Mol Cell Cardiol* **53**, 187-195 (2012).
25. M. Itoh, K. Ishihara, N. Nakashima, M. Takano, The hyperpolarization-activated cyclic nucleotide-gated (HCN) channels contain multiple S-palmitoylation sites. *J Physiol Sci* **66**, 241-248 (2016).

26. B. P. Head *et al.*, Microtubules and actin microfilaments regulate lipid raft/caveolae localization of adenylyl cyclase signaling components. *J Biol Chem* **281**, 26391-26399 (2006).

27. S. R. Agarwal *et al.*, Compartmentalized cAMP Signaling Associated With Lipid Raft and Non-raft Membrane Domains in Adult Ventricular Myocytes. *Front Pharmacol* **9**, 332 (2018).

28. L. J. Handlin, G. Dai, Direct regulation of the voltage-sensing domain of HCN channels by membrane lipid compartmentalization. *bioRxiv* https://doi.org/10.1101/2023.06.15.545112 (2023).

29. A. Saponaro *et al.*, Gating movements and ion permeation in HCN4 pacemaker channels. *Mol Cell* **81**, 2929-2943 e2926 (2021).

30. M. D. Clark, G. F. Contreras, R. Shen, E. Perozo, Electromechanical coupling in the hyperpolarization-activated K^+ channel KAT1. *Nature* 10.1038/s41586-020-2335-4 (2020).

31. P. A. M. Schmidpeter *et al.*, Anionic lipids unlock the gates of select ion channels in the pacemaker family. *Nat Struct Mol Biol* **29**, 1092-1100 (2022).

32. P. Pian, A. Bucchi, A. Decostanzo, R. B. Robinson, S. A. Siegelbaum, Modulation of cyclic nucleotide-regulated HCN channels by PIP_2 and receptors coupled to phospholipase C. *Pflugers Arch* **455**, 125-145 (2007).

33. T. Matsubara *et al.*, Heterogeneous Ganglioside-Enriched Nanoclusters with Different Densities in Membrane Rafts Detected by a Peptidyl Molecular Probe. *Langmuir* **37**, 646-654 (2021).

34. R. Sachl *et al.*, On multivalent receptor activity of GM1 in cholesterol containing membranes. *Biochim Biophys Acta* **1853**, 850-857 (2015).

35. G. W. Feigenson, T. A. Enoki, Nano-scale domains in the plasma membrane are like macroscopic domains in asymmetric bilayers. *Biophys J* **122**, 925-930 (2023).

36. F. Huang *et al.*, Multiple conformations of full-length p53 detected with single-molecule fluorescence resonance energy transfer. *Proc Natl Acad Sci U S A* **106**, 20758-20763 (2009).

37. M. A. Digman, V. R. Caiolfa, M. Zamai, E. Gratton, The phasor approach to fluorescence lifetime imaging analysis. *Biophys J* **94**, L14-16 (2008).

38. E. Hinde, M. A. Digman, K. M. Hahn, E. Gratton, Millisecond spatiotemporal dynamics of FRET biosensors by the pair correlation function and the phasor approach to FLIM. *Proc Natl Acad Sci U S A* **110**, 135-140 (2013).

39. L. Malacrida, S. Ranjit, D. M. Jameson, E. Gratton, The Phasor Plot: A Universal Circle to Advance Fluorescence Lifetime Analysis and Interpretation. *Annu Rev Biophys* **50**, 575-593 (2021).
40. S. Ranjit, L. Malacrida, D. M. Jameson, E. Gratton, Fit-free analysis of fluorescence lifetime imaging data using the phasor approach. *Nat Protoc* **13**, 1979-2004 (2018).
41. V. Lariccia *et al.*, Massive calcium-activated endocytosis without involvement of classical endocytic proteins. *J Gen Physiol* **137**, 111-132 (2011).
42. D. W. Hilgemann, M. Fine, M. E. Linder, B. C. Jennings, M. J. Lin, Massive endocytosis triggered by surface membrane palmitoylation under mitochondrial control in BHK fibroblasts. *Elife* **2**, e01293 (2013).
43. R. V. Haberberger, C. Barry, N. Dominguez, D. Matusica, Human Dorsal Root Ganglia. *Front Cell Neurosci* **13**, 271 (2019).
44. M. F. Esposito, R. Malayil, M. Hanes, T. Deer, Unique Characteristics of the Dorsal Root Ganglion as a Target for Neuromodulation. *Pain Med* **20**, S23-S30 (2019).
45. X. Zeng *et al.*, Oleic acid ameliorates palmitic acid induced hepatocellular lipotoxicity by inhibition of ER stress and pyroptosis. *Nutr Metab (Lond)* **17**, 11 (2020).
46. P. Hirsova, S. H. Ibrabim, G. J. Gores, H. Malhi, Lipotoxic lethal and sublethal stress signaling in hepatocytes: relevance to NASH pathogenesis. *J Lipid Res* **57**, 1758-1770 (2016).
47. T. Kayano *et al.*, Chronic NGF treatment induces somatic hyperexcitability in cultured dorsal root ganglion neurons of the rat. *Biomed Res* **34**, 329-342 (2013).
48. R. Zajaczkowska *et al.*, Mechanisms of Chemotherapy-Induced Peripheral Neuropathy. *Int J Mol Sci* **20** (2019).
49. C. Dart, Lipid microdomains and the regulation of ion channel function. *J Physiol* **588**, 3169-3178 (2010).
50. Y. Li *et al.*, DRG Voltage-Gated Sodium Channel 1.7 Is Upregulated in Paclitaxel-Induced Neuropathy in Rats and in Humans with Neuropathic Pain. *J Neurosci* **38**, 1124-1136 (2018).
51. G. Dai, Neuronal KCNQ2/3 channels are recruited to lipid raft microdomains by palmitoylation of BACE1. *J Gen Physiol* **154** (2022).
52. I. Decosterd, C. J. Woolf, Spared nerve injury: an animal model of persistent peripheral neuropathic pain. *Pain* **87**, 149-158 (2000).

53. E. Cavalli, S. Mammana, F. Nicoletti, P. Bramanti, E. Mazzon, The neuropathic pain: An overview of the current treatment and future therapeutic approaches. *Int J Immunopathol Pharmacol* **33**, 2058738419838383 (2019).

54. L. Colloca *et al.*, Neuropathic pain. *Nat Rev Dis Primers* **3**, 17002 (2017).

55. O. van Hecke, S. K. Austin, R. A. Khan, B. H. Smith, N. Torrance, Neuropathic pain in the general population: a systematic review of epidemiological studies. *Pain* **155**, 654-662 (2014).

56. J. C. DiFrancesco, D. DiFrancesco, Dysfunctional HCN ion channels in neurological diseases. *Front Cell Neurosci* **6**, 174 (2015).

57. C. Tsantoulas, E. R. Mooney, P. A. McNaughton, HCN2 ion channels: basic science opens up possibilities for therapeutic intervention in neuropathic pain. *Biochem J* **473**, 2717-2736 (2016).

58. A. Pristera, M. D. Baker, K. Okuse, Association between tetrodotoxin resistant channels and lipid rafts regulates sensory neuron excitability. *PLoS One* **7**, e40079 (2012).

59. S. H. Park, S. J. Opella, Tilt angle of a trans-membrane helix is determined by hydrophobic mismatch. *J Mol Biol* **350**, 310-318 (2005).

60. T. Kim, W. Im, Revisiting hydrophobic mismatch with free energy simulation studies of transmembrane helix tilt and rotation. *Biophys J* **99**, 175-183 (2010).

61. G. Dai, T. K. Aman, F. DiMaio, W. N. Zagotta, Electromechanical coupling mechanism for activation and inactivation of an HCN channel. *Nat Commun* **12**, 2802 (2021).

62. G. Dai, H. Yu, M. Kruse, A. Traynor-Kaplan, B. Hille, Osmoregulatory inositol transporter SMIT1 modulates electrical activity by adjusting PI(4,5)P_2 levels. *Proc Natl Acad Sci U S A* **113**, E3290-3299 (2016).

63. R. A. Colyer, C. Lee, E. Gratton, A novel fluorescence lifetime imaging system that optimizes photon efficiency. *Microsc Res Tech* **71**, 201-213 (2008).

64. G. Dai, W. N. Zagotta, Molecular mechanism of voltage-dependent potentiation of KCNH potassium channels. *Elife* **6** (2017).

65. K. S. McCommis *et al.*, Loss of Mitochondrial Pyruvate Carrier 2 in the Liver Leads to Defects in Gluconeogenesis and Compensation via Pyruvate-Alanine Cycling. *Cell Metab* **22**, 682-694 (2015).

66. S. Fenske *et al.*, Comprehensive multilevel in vivo and in vitro analysis of heart rate fluctuations in mice by ECG telemetry and electrophysiology. *Nat Protoc* **11**, 61-86 (2016).

67. A. Moutal *et al.*, SARS-CoV-2 spike protein co-opts VEGF-A/neuropilin-1 receptor signaling to induce analgesia. *Pain* **162**, 243-252 (2021).

68. A. Moutal *et al.*, CRMP2-Neurofibromin Interface Drives NF1-related Pain. *Neuroscience* **381**, 79-90 (2018).

69. A. Moutal *et al.*, CRISPR/Cas9 editing of Nf1 gene identifies CRMP2 as a therapeutic target in neurofibromatosis type 1-related pain that is reversed by (S)-Lacosamide. *Pain* **158**, 2301-2319 (2017).

70. A. Moutal *et al.*, (S)-lacosamide inhibition of CRMP2 phosphorylation reduces postoperative and neuropathic pain behaviors through distinct classes of sensory neurons identified by constellation pharmacology. *Pain* **157**, 1448-1463 (2016).